

# General Oriented Formation of Carbon Nanotubes from Metal–Organic Frameworks

Jiashen Meng,<sup>†,‡</sup> Chaojiang Niu,<sup>†,‡</sup> Linhan Xu,<sup>‡,‡</sup> Jiantao Li,<sup>†</sup> Xiong Liu,<sup>†</sup> Xuanpeng Wang,<sup>†</sup> Yuzhu Wu,<sup>†</sup> Xiaoming Xu,<sup>†</sup> Wenyi Chen,<sup>†</sup> Qi Li,<sup>†</sup> Zizhong Zhu,<sup>\*,‡,§</sup> Dongyuan Zhao,<sup>†,§</sup> and Liqiang Mai<sup>\*,†,§</sup>

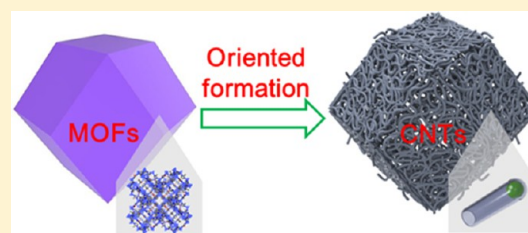
<sup>†</sup>State Key Laboratory of Advanced Technology for Materials Synthesis and Processing, Wuhan University of Technology, Wuhan 430070, China

<sup>‡</sup>Department of Physics and Collaborative Innovation Center for Optoelectronic Semiconductors and Efficient Devices, Xiamen University, Xiamen 361005, China

<sup>§</sup>Department of Chemistry, University of California, Berkeley, California 94720, United States

## Supporting Information

**ABSTRACT:** Carbon nanotubes (CNTs) are of great interest for many potential applications because of their extraordinary electronic, mechanical and structural properties. However, issues of chaotic staking, high cost and high energy dissipation in the synthesis of CNTs remain to be resolved. Here we develop a facile, general and high-yield strategy for the oriented formation of CNTs from metal–organic frameworks (MOFs) through a low-temperature (as low as 430 °C) pyrolysis process. The selected MOF crystals act as a single precursor for both nanocatalysts and carbon sources. The key to the formation of CNTs is obtaining small nanocatalysts with high activity during the pyrolysis process. This method is successfully extended to obtain various oriented CNT-assembled architectures by modulating the corresponding MOFs, which further homogeneously incorporate heteroatoms into the CNTs. Specifically, nitrogen-doped CNT-assembled hollow structures exhibit excellent performances in both energy conversion and storage. On the basis of experimental analyses and density functional theory simulations, these superior performances are attributed to synergistic effects between ideal components and multilevel structures. Additionally, the appropriate graphitic N doping and the confined metal nanoparticles in CNTs both increase the densities of states near the Fermi level and reduce the work function, hence efficiently enhancing its oxygen reduction activity. The viable synthetic strategy and proposed mechanism will stimulate the rapid development of CNTs in frontier fields.



## INTRODUCTION

Carbon nanotubes (CNTs), an important allotrope of carbon, have cylindrical structures with diameters ranging from one to tens of nanometers and lengths ranging from a few micrometers to several centimeters.<sup>1</sup> Over the past few decades, CNTs have shown great potential in logic circuits, gas storage, catalysis and energy storage because of their extraordinary electronic, mechanical and structural properties.<sup>2–5</sup> Intensive efforts have also been devoted to developing efficient strategies for the synthesis of CNTs, such as arc discharge, laser ablation and chemical vapor deposition methods, among others.<sup>6–9</sup> Despite great advancements in their synthesis, high costs and high energy dissipation continue to limit CNTs' further applications. Because of the harsh synthetic conditions (e.g., >800 °C), the preparation of uniformly disperse CNTs is difficult. Bottom-up organic synthesis has recently been demonstrated to be a promising approach to prepare CNTs with the precise control of diameter and length under facile conditions.<sup>10,11</sup> Selective organic molecules, acting as basic units, can form predicted CNTs after polymerization. However, this precisely synthetic method is limited by low yields and a complex synthetic process. In addition, Shrestha et al. recently

reported similar interesting cubic nanocarbon structures, enhancing their electrochemical activity for energy storage.<sup>12,13</sup>

For further potential application of CNTs, better control over the building and organization of CNT-based architectures is needed in the manufacture of electromechanical devices.<sup>14</sup> What's more, as another factor, the introduction of heteroatoms (N, B, P, etc.) into CNTs can cause electron modulation, resulting in more novel applications, especially including electrocatalysis.<sup>15,16</sup> Therefore, the development of a facile and general strategy for the synthesis of CNTs with high yield, organized assembly and precise dopant control is highly desired for practical applications.

Metal–organic frameworks (MOFs), a new class of porous crystalline materials, have attracted enormous attentions in many applications over the past two decades because of their high surface area, tunable porosity and controllable structures.<sup>17–20</sup> By varying the metal ions/clusters and organic linkers, researchers can assemble and create different functional MOFs via coordination bonds.<sup>21</sup> Recently, MOFs have been

Received: February 24, 2017

Published: May 25, 2017

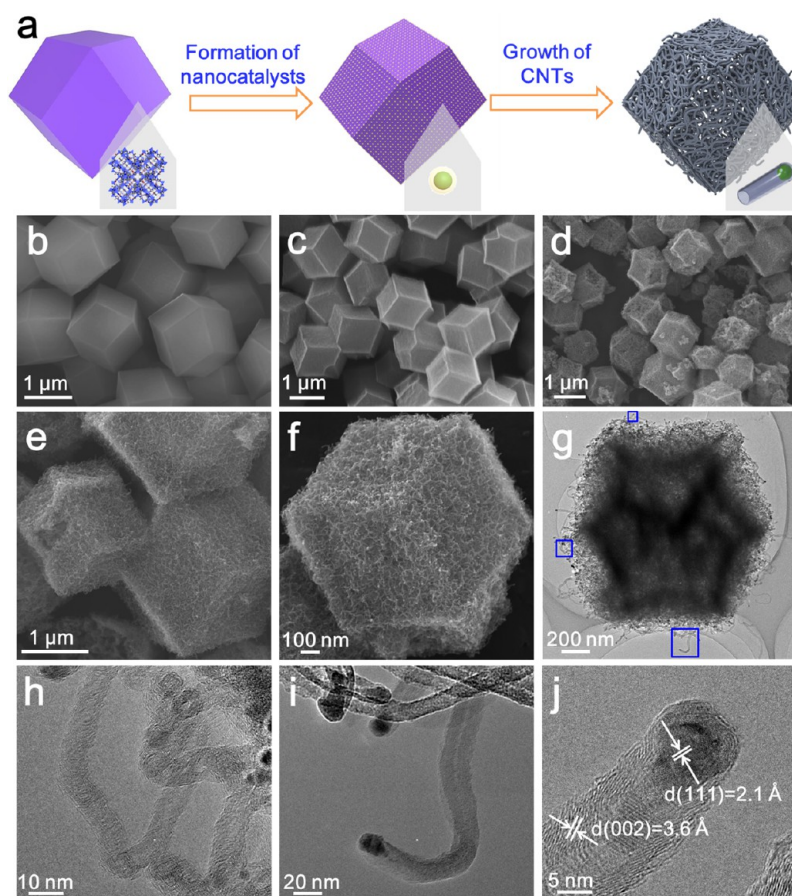


**Figure 1.** Synthesis and characterization of N-doped CNT-assembled hollow dodecahedra from zeolitic imidazolate frameworks (ZIF-67). (a) Schematics of the formation process of N-CNTs from ZIF-67. During the pyrolysis of ZIF-67 at 435 °C under argon, the nanocatalysts are formed on the outer surfaces; the growth of N-CNTs is subsequently catalyzed on the nanocatalysts, finally obtaining N-CNT-assembled hollow dodecahedra. (b–d) The corresponding SEM images of fresh ZIF-67 (b) and samples prepared after low-temperature pyrolysis at 435 °C in argon for 0.5 h (c) and 8 h (d), respectively. (e–j) SEM, TEM and HRTEM images of N-CNT-assembled hollow dodecahedra.

reported as promising candidates for carbon-based materials.<sup>22–24</sup> Lou et al. reported the preparation of N-doped CNTs (N-CNTs) with excellent electrocatalytic activity via high-temperature pyrolysis (>600 °C) of zeolitic imidazolate frameworks (ZIFs) in the presence of H<sub>2</sub>.<sup>25</sup> Xu et al. developed a self-templated strategy for the synthesis of carbon nanorods with superior supercapacitor performance from rod-shaped MOFs (1000 °C, argon atmosphere).<sup>26</sup> Despite great advancements in the energy conversion and storage fields, these MOF-derived carbon-based materials are limited by high-temperature pyrolysis and/or simple structures (e.g., solid interiors and/or solid shells), which hinder their further applications. Therefore, the synthesis of multilevel CNT-assembled structures from various MOFs by a low-temperature and general method remains a formidable challenge.

Herein, we design a facile and high-yield strategy for the general oriented formation of CNTs from MOFs via a low-temperature (as low as 430 °C) pyrolysis process. During the pyrolysis process, the generated reducing gases first turn metal ions/clusters into metal nanocatalysts; these nanocatalysts then further catalyze the residual organic units to form CNTs. This strategy can be generally applied to obtain different morphology-preserved CNT-assembled structures through the modulation of MOFs. These as-prepared architectures possess a high specific surface area, controlled dopants, hierarchical pores and stable frameworks, hence resulting in high activity,

fast mass transport and good strain accommodation (Figure S1). Consequently, when applied in energy conversion and storage, these architectures assembled with metal and/or metal oxide nanoparticles encapsulated into N-CNTs exhibit excellent performance as oxygen reduction reaction (ORR) catalysts and as lithium-ion-battery (LIB) anode materials. The detailed experimental analyses and density functional theory simulations demonstrate that the synergistic effect between the appropriate N doping and confined metal nanoparticles endows this architecture with outstanding electrochemical performance. This understanding gives further insights into the structure–property correlation of metal nanoparticles confined in N-CNTs.

## RESULTS AND DISCUSSION

The overall synthetic procedure for N-CNTs from ZIF-67 is presented in Figure 1a. The ZIF-67 dodecahedron crystals with micrometer size are first synthesized at room temperature.<sup>27</sup> The crystals exhibit uniform morphology, high crystallinity and high specific surface area (1389 m<sup>2</sup> g<sup>-1</sup>) (Figure 1b and Figure S2). Then, ZIF-67 dodecahedra are treated at a low temperature of 435 °C under argon. The coordination bonds between metal ions and organic ligands in the ZIF-67 dodecahedra break first because of their longer binding length (Figure S3). The pyrolysis process is explored by thermogravimetric analysis (TGA)-mass spectrometry (MS), along with

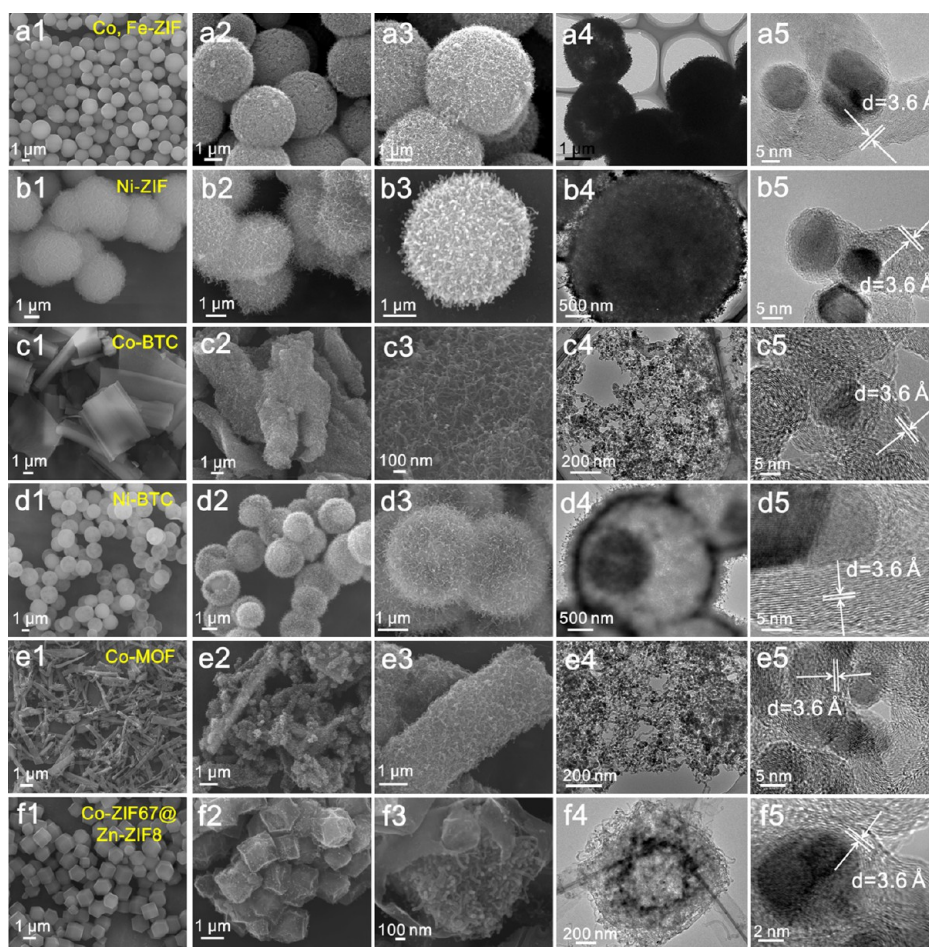


**Figure 2.** The broad extension of the oriented formation method. (a1) SEM image of the Co, Fe-ZIF precursor. (a2–a5) SEM, TEM and HRTEM images of the Co, Fe-ZIF-derived N-CNT-assembled microspheres; (b1) SEM image of the Ni-ZIF precursor. (b2–b5) SEM, TEM and HRTEM images of the Ni-ZIF-derived N-CNT-assembled microspheres; (c1) SEM image of the Co-BTC precursor. (c2–c5) SEM, TEM and HRTEM images of the Co-BTC-derived CNT-assembled microsheets; (d1) SEM image of the Ni-BTC precursor. (d2–d5) SEM, TEM and HRTEM images of the Ni-BTC-derived CNT-assembled hollow microspheres; (e1) SEM image of the Co-MOF precursor. (e2–e5) SEM, TEM and HRTEM images of the Co-MOF-derived CNT-assembled nanorods; (f1) SEM image of the Co-ZIF-67@Zn-ZIF-8 precursor. (f2–f5) SEM, TEM and HRTEM images of the Co-ZIF-67@Zn-ZIF-8-derived N-CNT-assembled core–shell dodecahedra.

energy changes and gas release ( $\text{NH}_3$  and  $\text{H}_2$ ) (Figure S4). The corresponding mass loss is about 30 wt %. These gases can reduce metal ions into metals, facilitating the nucleation of nanocatalysts. After 0.5 h of pyrolysis, the surfaces of the ZIF-67 dodecahedra become rough, indicating the preliminary formation of nanocatalysts (Figure 1c and Figure S5). In addition, the organic residuals do not volatilize and surround the nanocatalysts. Similar to the aforementioned bottom-up organic method, organic residuals acting as basic units are catalyzed into N-CNTs on the nanocatalysts. Because of the preferential formation of metal nanocrystals on the surface and the subsequent growth of N-CNTs thereupon, the growth direction is from inside to outside, leading to hollow interior voids. Eventually, after complete pyrolysis, hollow dodecahedra are obtained, which are morphology-preserved and composed of thin N-CNTs with Co nanoparticles inside them (Figure 1d). During the pyrolysis process, the ZIF-67 dodecahedra as a single precursor oriented the in situ formation of N-CNTs, and were eventually converted into morphology-preserved N-CNT-assembled structures. In brief, the oriented formation process undergoes the pyrolysis of MOFs, the formation of nanocatalysts and the growth of CNTs, which can be applied to various MOFs. Moreover, our strategy can realize lower-

temperature synthesis (as low as 435 °C) and greater productivity (up to 70 wt %) of N-CNTs than the traditional solid-phase method (900 °C and 2.5 wt %) (Figures S6 and S7).

The hollow dodecahedra are uniform with an average size of  $\sim 1 \mu\text{m}$ , which are composed of thin N-CNTs (Figure 1e, f). The interior hollow voids are also demonstrated by broken dodecahedra (Figures S8 and S9). These thin N-CNTs have outer diameters ranging from 10 to 20 nm and inner diameters of  $\sim 5 \text{ nm}$ , showing a multiwalled feature (Figure 1g–j). Crystalline cobalt nanoparticles of  $\sim 5 \text{ nm}$  are encapsulated into the top of the N-CNTs. Small graphitic layers with interlayer spacings of  $\sim 3.6 \text{ \AA}$  are randomly stacked in the walls and are not parallel to the axis direction, exhibiting more defects and edges in the N-CNTs. Raman characteristic signatures located at approximately  $1350$  and  $1600 \text{ cm}^{-1}$  are attributed to the D band (originating from disoriented carbon) and the G band (graphitic carbon), respectively (Figure S8d). A high  $I_D/I_G$  band intensity ratio reveals large amounts of defects in the N-CNTs, consistent with the TEM observations. The elemental analysis results indicate that the mass contents of C, N and H in the pure N-CNTs are approximately 70.5, 25.5, and 4.0 wt %, respectively (Table S1). To our knowledge, the N content in

our carbon nanotubes is higher than that in the N-CNTs reported previously because of the low temperature of formation. X-ray photoelectron spectroscopy (XPS) and energy-dispersive X-ray spectroscopy (EDS) analysis confirm the presence and distribution of Co, C and N (Figure S8c, g). Furthermore, the high-resolution N 1s XPS spectrum was deconvoluted into three types of nitrogen species: pyridinic N (398.4 eV, 38.1%), pyrrolic N (399.8 eV, 45.6%) and graphitic N (400.7 eV, 16.3%), which have different effects on adjacent carbon rings (Figure S10).<sup>28</sup> The nitrogen adsorption–desorption analysis shows a high Brunauer–Emmett–Teller (BET) specific surface area of 268 m<sup>2</sup> g<sup>-1</sup> (Figure S8e, f). The pore size distribution is mainly below 4 nm because of the random and loose stacking of tiny graphitic layers in the N-CNTs.

To confirm the versatility of our strategy, various delicate morphology-preserved CNT-assembled structures from MOFs were also obtained according to the aforementioned mechanism (Figure 2). First, various MOF crystals with different morphologies and components were synthesized by facile solution methods, including Co, Fe-ZIF microspheres, Ni-ZIF microspheres, Co-BTC microspheres, Ni-BTC hollow microspheres, Co-MOF nanorods and Co-ZIF-67@Zn-ZIF-8 dodecahedra (Figures S11–S16).<sup>29–32</sup> The detailed processes are illustrated in the Experimental Section. SEM images show that these obtained MOFs possess smooth surfaces and coincident morphologies. The corresponding XRD patterns show high crystallinity. Subsequently, when these as-synthesized MOFs were treated at a low pyrolysis temperature, the morphology-preserved CNT-assembled architectures were obtained after sufficient pyrolysis. TEM images give more direct evidence for the oriented CNT-assembled structures, most of which exhibit hollow structures. These CNTs are composed of layered graphitic carbon with clear interlayer spacings of ~3.6 Å, and different metal nanocatalysts are encapsulated into the CNTs. Additional SEM images, EDS mappings and corresponding XRD patterns of each sample are also presented. Some broken CNT-assembled architectures clearly reveal the cross-section and inside structures (Figure S17). Interestingly, because of the lack of heteroatom doping, the CNTs from the Ni-BTC, Co-BTC, and Co-MOF precursors possess successive and integrated graphitic layers, which are parallel to the axis direction. Their XRD patterns show high graphitization and clear diffraction peaks from graphitic carbon. Overall, this strategy can be widely applied to synthesize oriented CNT-assembled architectures with tunable morphologies, components and doping. Compared with other reported methods for high-quality CNTs, our strategy for the synthesis of unique CNT-assembled structures shows great potential in the development of CNTs in many frontier fields (Table S2).

In our strategy, the use of MOFs as single precursors is of great importance in the formation of CNTs. First, the derived metal nanocatalysts play an important role in the formation of CNTs. After complete pyrolysis of the core–shell Co-ZIF-67@Zn-ZIF-8 dodecahedra, the inner core forms the N-CNTs, whereas the outer shell is carbon-based frameworks. This difference is ascribed to the formation and catalytic activity of metal nanocatalysts during the pyrolysis process. The corresponding XRD patterns are well indexed to the pure phase of the Co nanocatalysts, indicating an easy formation from Co-ZIF-67. By contrast, after complete pyrolysis of Zn-ZIF-8 dodecahedra even at 600 °C, the product remains in the zinc oxide phase (Figure S18). Therefore, the derived

nanocatalysts should easily form and should exhibit high catalytic activity, usually including Co, Fe and Ni. Second, carbon sources also greatly influence the formation of CNTs. Rich hexatomic or N-heterocyclic carbon rings from organic ligands can directly act as basic units of CNTs and reduce cyclization energy barriers, resulting in the easy formation of CNTs. Finally, the high crystallinity of MOFs is another key point. During the pyrolysis, the energy and gas released from broken coordination bonds in highly crystalline MOFs can stimulate high activation of organic residuals and metal ions/clusters, thereby facilitating the formation of nanocatalysts and the growth of CNTs (Figure S19). To confirm this effect, amorphous organic–inorganic precursor microspheres were synthesized and compared (Figure S20). However, after pyrolysis under similar conditions, the derived microspheres were aggregated as obvious particles instead of existing as CNTs. Overall, selected MOFs should fulfill three prerequisites as ideal precursors: (1) easy formation of highly active nanocatalysts from metal ions/clusters, (2) rich hexatomic or N-heterocyclic carbon rings in organic ligands as basic units of CNTs, and (3) high crystallinity.

Additionally, controlled pyrolysis is crucial in obtaining CNTs, involving the holding temperature and time. In our strategy, the holding temperatures are near the decomposition temperatures of selected MOFs, and the corresponding pyrolysis rates are very slow, which can form small nanocatalysts and facilitate the growth of CNTs. The binding energy of coordination bonds in selected MOFs greatly influences the corresponding pyrolysis temperatures. Because of the slow pyrolysis kinetics, a sufficient holding time is critical for the complete pyrolysis of MOFs. However, during high-temperature treatment, the pyrolysis rates become very high, accelerating the corresponding kinetics processes, thereby affecting the formation of CNTs. After treatment at 500 °C, the ZIF-67, Ni-BTC and Co-BTC precursors could not generate CNTs (Figure S21). These structures retained the morphologies of precursors and were composed of relatively large nanoparticles. According to a statistical analysis, these nanoparticles contained metal cores of ~12 nm in diameter and carbon shells of ~3 nm in thickness. Large metal cores have low activity and cannot catalyze surrounding carbon shells into CNTs. By contrast, Lou et al. have reported N-CNTs derived from ZIF-67 at a higher holding temperature (>600 °C) because H<sub>2</sub> can reduce metal ions to generate more crystal nuclei, resulting in the formation of small nanocatalysts.<sup>25</sup> Generally, the diameters of nanocatalysts play a critical role in the inner diameters of CNTs. Therefore, the key point for the formation of CNTs from selected MOFs is obtaining small nanocatalysts with high activity during the pyrolysis process.

The nitrogen contents and species in carbon-based materials are crucial in their ORR performance.<sup>33–36</sup> To investigate these effects, the as-synthesized N-CNTs sample (denoted as N-CNTs-435) was treated at different temperatures (550, 650, and 750 °C), thereby resulting in N-CNTs-550, N-CNTs-650 and N-CNTs-750 samples, respectively. These samples still exhibit similar integrated morphologies (Figure S22). First, we performed cyclic voltammetry (CV) measurements in O<sub>2</sub>-saturated 0.1 M KOH solution (Figure S23). The N-CNTs-650 sample exhibits a marked oxygen reduction peak at 0.87 V versus reversible hydrogen electrode (RHE), which is more positive than those of N-CNTs-435 (0.81 V), N-CNTs-550 (0.86 V) and N-CNTs-750 (0.84 V). From linear sweep voltammetry (LSV) curves in rotating disk electrode (RDE)

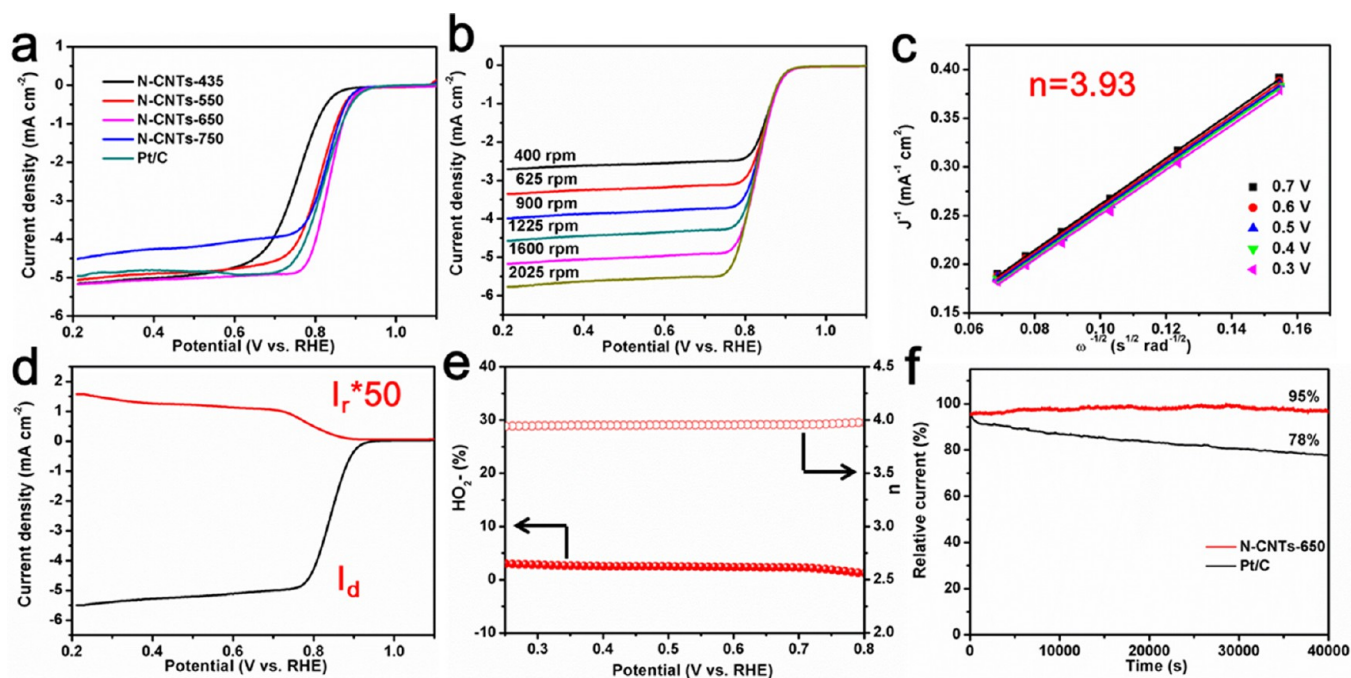


**Figure 3.** ORR electrocatalytic performances of metal nanoparticles encapsulated into N-CNTs. (a) LSV curves of N-CNTs-435, N-CNTs-550, N-CNTs-650, N-CNTs-750 and Pt/C in  $O_2$ -saturated 0.1 M KOH at a scan rate of  $5 \text{ mV}\cdot\text{s}^{-1}$  and 1600 rpm. (b) LSV curves of N-CNTs-650 in  $O_2$ -saturated 0.1 M KOH at a scan rate of  $5 \text{ mV}\cdot\text{s}^{-1}$  and different rotation rates. (c) K-L plots of N-CNTs-650 at different potentials. (d) RRDE voltammograms recorded with N-CNTs-650 in  $O_2$ -saturated 0.1 M KOH at 1600 rpm. (e) Peroxide yields and electron numbers of N-CNTs-650 at various potentials based on RRDE data. (f) Chronoamperometric (current–time) responses of N-CNTs-650 and Pt/C in  $O_2$ -saturated 0.1 M KOH at 1600 rpm and 0.7 V versus RHE.

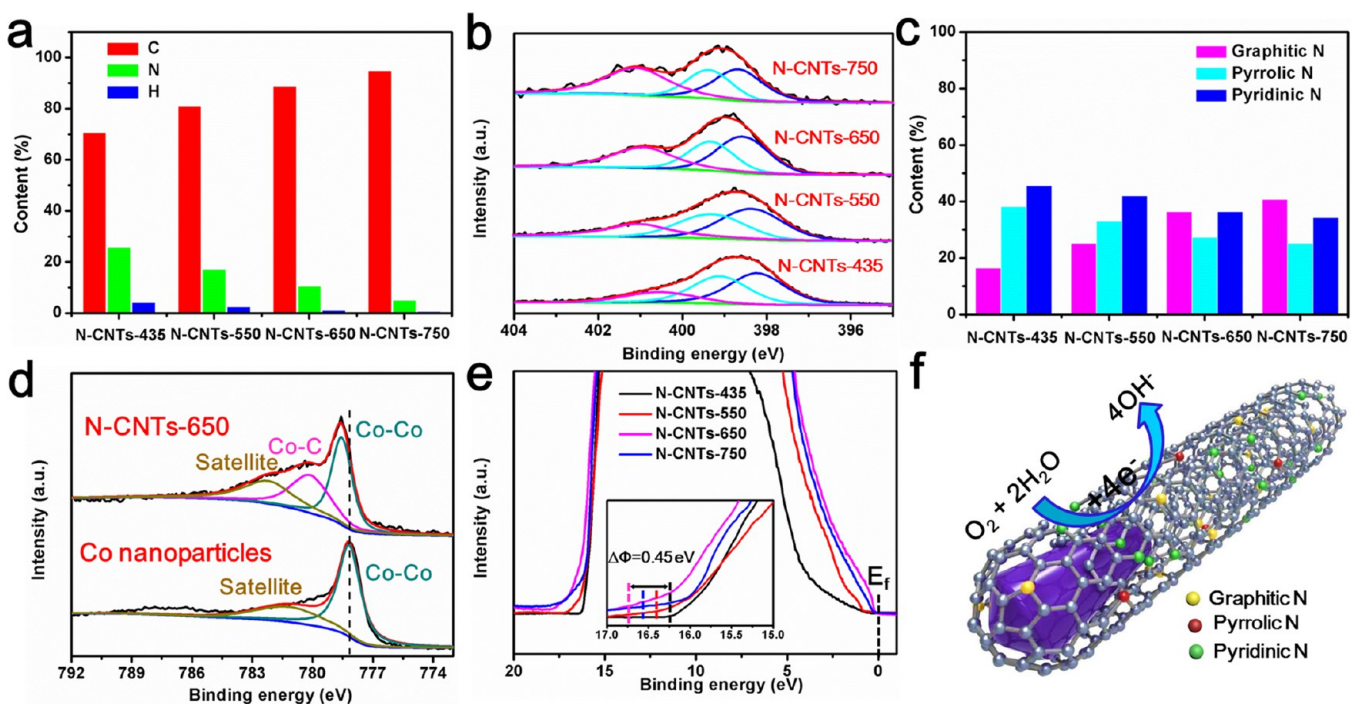


**Figure 4.** Characterizations of various N-CNTs samples. (a) The relative contents of C, N and H in N-CNTs-435, N-CNTs-550, N-CNTs-650, and N-CNTs-750. (b) High-resolution N 1s XPS spectra of N-CNTs-435, N-CNTs-550, N-CNTs-650, and N-CNTs-750. (c) The corresponding contents of pyridinic N, pyrrolic N and graphitic N. (d) High-resolution Co  $2p_{3/2}$  XPS spectra of Co nanoparticles and N-CNTs-650. (e) UPS spectra collected using He I (21.2 eV) radiation. Inset shows the enlarged view of the secondary electron tail threshold. (f) Schematic of Co confined in N-CNTs for the ORR process.

experiments at 1600 rpm, the N-CNTs-650 sample shows a half-wave potential ( $E_{1/2}$ ) of 0.85 V versus RHE (Figure 3a).

This value is more positive than those of the N-CNTs-435 (0.75 V), N-CNTs-550 (0.82 V), N-CNTs-750 (0.83 V) and

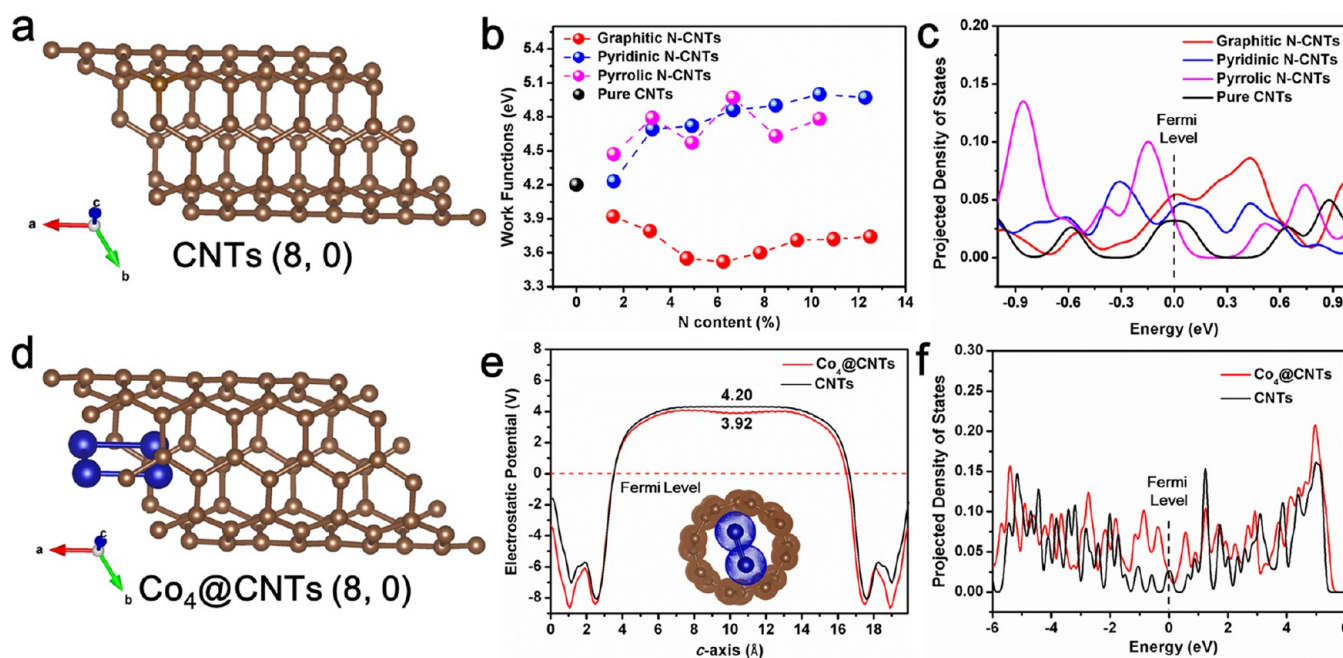


**Figure 5.** Results of DFT simulations on CNTs, N-CNTs and  $\text{Co}_4$ @CNTs. (a) Schematic model of single-walled CNTs (8, 0). (b) Work function summary of pure CNTs and N-CNTs with different nitrogen species (graphitic N, pyridinic N and pyrrolic N) and various contents of nitrogen species (0–15%). (c) Calculated total densities of states of pure CNTs, graphitic N-CNTs, pyridinic N-CNTs and pyrrolic N-CNTs near the Fermi level with the Fermi level aligned at 0 eV. (d) Schematic of  $\text{Co}_4$ @CNTs (8, 0). (e) Calculated electrostatic potential profile averaged on the plane perpendicular to the  $c$ -axis as a function of the  $b$ -axis of pure CNTs and  $\text{Co}_4$ @CNTs. The Fermi level is aligned at 0 eV. The inset of (e) is the sectional view of (d), showing the electron interactions between the inner  $\text{Co}_4$  nanoclusters and outer CNTs. (f) Calculated total densities of states of pure CNTs and  $\text{Co}_4$ @CNT with the Fermi level aligned at 0 eV.

Pt/C (0.83 V). Additionally, the N-CNTs-650 sample exhibits a higher current density and a more apparent plateau of diffusion-limiting current because of greater electrocatalytic activity toward the ORR process.<sup>37</sup> RDE experiments at different rotating rates were carried out, and the corresponding kinetic parameters were analyzed with the Koutecky–Levich (K–L) equation (Figure 3b, c). The linearity of the K–L plots indicates first-order reaction kinetics with regard to the concentration of dissolved oxygen and similar electron transfer numbers ( $n$ ) at various potentials.<sup>38</sup> The  $n$  value of N-CNTs-650 is  $\sim 3.93$ , suggesting an apparent  $4e^-$  ORR pathway. Moreover, the ORR catalytic behaviors were evaluated by the  $n$  and by the yield of peroxide species ( $\text{HO}_2^-$ ) from the rotational ring-disk electrodes (RRDE) measurement (Figure 3d). The  $\text{H}_2\text{O}_2$  yield on the N-CNTs-650 sample is calculated to be less than 4% in the potential range from 0.25 to 0.8 V, and the calculated  $n$  is  $\sim 3.94$ , which is similar to the results obtained from the K–L plots (Figure 3e). Furthermore, chronoamperometric responses were measured to evaluate the durability of N-CNTs-650 and Pt/C at 0.7 V and 1600 rpm (Figure 3f). The N-CNTs-650 sample presents excellent long-term stability with 95% current retention after 40000 s, which is much better than the commercial Pt/C catalyst (78% current retention). Compared with bare Co nanoparticles in the absence of the N-CNTs, the superior ORR electrocatalytic performances of N-CNTs-650 are attributed to the structural merits (Figure S24). The N-CNTs-650 sample exhibits excellent electrocatalytic activity for the ORR performance among numerous reported electrocatalysts (Table S3).

On the basis of both XRD and Raman analyses, the graphitization degree of the N-CNTs samples increases with heating temperature, which is beneficial for high electronic

mobility (Figure S25). The nitrogen mass contents in N-CNTs-435, N-CNTs-550, N-CNTs-650 and N-CNTs-750 are 25.5, 16.9, 10.5, and 4.9 wt %, respectively (Figure 4a). The relative contents of graphitic N gradually increase from N-CNTs-435 to N-CNTs-750, whereas both pyridinic N and pyrrolic N decrease (Figure 4b, c). On the basis of the aforementioned analysis, the N-CNTs-650 sample exhibits an appropriate nitrogen content and a relatively high ratio of graphitic-N, leading to its balance between the contents and species of nitrogen. This balance can realize both the relatively higher electronic mobility and more active sites in N-CNTs-650, which are beneficial for electrocatalytic activity.<sup>39</sup> On the other hand, confined Co nanoparticles have interacted with N-CNT shells and affected the properties of the outer walls, where  $\text{O}_2$  is activated and reduced. Previous studies have shown that the strong interaction between metal nanoparticles and CNTs can facilitate electron transfer from the metal atoms to CNTs, thereby accelerating the formation of the OOH species.<sup>40</sup> High-resolution Co  $2p_{3/2}$  spectra of N-CNTs-650 can be deconvoluted into two peaks at 778.6 and 780.1 eV, corresponding to Co–Co and Co–C bonds, respectively (Figure 4d). In addition, the Co–Co bond peak shifts to a higher value than that of Co nanoparticles (778.1 eV). These phenomena demonstrate the strong interaction between N-CNTs and confined Co nanoparticles as well as the aforementioned electron transfer. The work functions ( $\Phi$ ) of N-CNTs-435, N-CNTs-550, N-CNTs-650 and N-CNTs-750 samples, as determined by ultraviolet photoelectron spectroscopy (UPS) are 4.83, 4.73, 4.45, and 4.58 eV, respectively (Figure 4e).<sup>41,42</sup> The N-CNTs-650 sample has the lowest work function, which is beneficial for donating electrons from the surface of N-CNTs to adsorbed molecular oxygen, thereby

facilitating the formation of OOH species. Therefore, as represented in the schematic in Figure 4f, the synergistic effect between N-CNTs and confined metal particles accelerates the ORR.

To elucidate this synergistic effect, we performed a series of DFT simulations (Figure 5 and Figures S26–S29). Models contain single-walled CNTs (8, 0), N-doped single-walled CNTs (N-CNTs) and Co<sub>4</sub> nanoclusters inside single-walled CNTs (Co<sub>4</sub>@CNTs) in our simulations. Although the sizes of Co nanoclusters and CNTs are much smaller than those observed experimentally, the essential effects on the electronic structures can be reasonably captured by these simple geometries. In previous reports, the work functions and densities of states (DOS) of carbon-based catalysts were used as effective parameters for predicting the ORR activity.<sup>43–46</sup> The properties of pure single-walled CNTs are characterized by DFT simulations and used as a comparison (Figure 5a and Figure S26). First, nitrogen species and contents play an important role in the electronic structures of CNTs. To clearly investigate these differences in electronic structures, we calculated various nitrogen species (graphitic N, pyridinic N and pyrrolic N) and contents (0–15%) in CNTs (Figure 5b). The work function values of graphitic N-CNTs are lower than that of pure CNTs. However, pyridinic N-CNTs and pyrrolic N-CNTs exhibit higher work function values than that of pure CNTs. By contrast, graphitic N-CNTs are more beneficial to the electron transfer, therefore enhancing the electrocatalytic performance.<sup>47</sup> Recently, Liu et al. reported that the graphitic-N and pyrrolic-N in graphene provide electrons to the  $\pi$ -conjugated system, whereas the electron-withdrawing pyridinic N in graphene accepts electrons from adjacent C atoms.<sup>42</sup> Generally, the electron-donating N sites of both graphitic N and pyrrolic N tend to lower the work function in N-CNTs. However, this difference can be attributed to the presence of more defects in pyrrolic N-CNTs, restricting the electron release and therefore leading to the work-function increase. Moreover, the values of graphitic N-CNTs first decrease and then increase along with the N content, which shows that the appropriate graphitic N doping is important for electrocatalysis. In addition, compared with pure CNTs, pyridinic N-CNTs (~6.67%) and pyrrolic N-CNTs (~6.67%), the calculated total DOS of selected graphitic N-CNTs with a similar N content (~6.25%) exhibits higher states in the characteristic low-DOS region near the Fermi level, indicating that O<sub>2</sub> can be readily adsorbed onto the graphitic N-CNTs (Figure 5c).

On the other hand, confined Co<sub>4</sub> nanoclusters also influence the electronic structures of CNTs (Figure 5d). The work function value of Co<sub>4</sub>@CNTs from DFT simulations is 3.92 eV, which is smaller than that of pure CNTs (4.2 eV) (Figure 5e). In addition, the corresponding calculated total DOS of Co<sub>4</sub>@CNTs shows more extra states near the Fermi level than the calculated total DOS of pure CNTs (Figure 5f). This reduced work function and increased DOS near the Fermi level are expected to enhance its chemical activity. These changes are attributed to the formation of local dipoles between confined Co<sub>4</sub> nanoclusters and outer CNTs, facilitating the electron transfer.<sup>40</sup> In brief, appropriate graphitic N doping and confined metal nanoparticles in CNTs can both increase the DOS near the Fermi level and reduce the work function, demonstrating a synergistic effect that endows the N-CNTs-650 sample with outstanding electrocatalytic performance in the ORR. This understanding grants further insights into the structure–property correlation of metal nanoparticles confined in N-

CNTs and provides a better direction for the design of ideal electrocatalysts for energy conversion.

To further reveal their structural superiority, Co<sub>3</sub>O<sub>4</sub> nanoparticles encapsulated into N-CNTs (denoted as Co<sub>3</sub>O<sub>4</sub>@N-CNTs) were obtained by the oxidation of N-CNTs-650 in air condition (Figures S30 and S31).<sup>48</sup> The scanning-TEM high-angle annular dark-field (STEM-HAADF) image and the TEM image confirmed the hollow CNT-assembled structures (Figure S30c–e). The STEM-EDS mappings further confirmed the distributions of doped elements and Co<sub>3</sub>O<sub>4</sub> on the CNT-assembled materials (Figure S30f–o). When employed as anodes for LIBs, the Co<sub>3</sub>O<sub>4</sub>@N-CNTs electrode can recover an approximately 100% after testing at various current densities from 0.1 to 5 A·g<sup>-1</sup> (Figure S32b). After 250 cycles at 0.1 A·g<sup>-1</sup>, the discharge capacity remains at 1030 mAh·g<sup>-1</sup> with a capacity retention of ~110% compared to the capacity of the second cycle (Figure S32c, d). However, the Co<sub>3</sub>O<sub>4</sub> nanoparticles in the absence of the N-CNTs exhibited a low discharge capacity of 331 mAh·g<sup>-1</sup> and a capacity retention of ~30% after 120 cycles at 0.1 A·g<sup>-1</sup> (Figure S33). Notably, even when measured at the high rate of 2 A·g<sup>-1</sup>, the Co<sub>3</sub>O<sub>4</sub>@N-CNTs remain stable after 1000 cycles, with capacity retention greater than 100% (Figure S30e). In addition, kinetic analysis and structural characterizations of Co<sub>3</sub>O<sub>4</sub>@N-CNTs present obvious lithiation pseudocapacitive behavior, fast electronic mobility and great structural stability in LIBs (Figures S34 and S35).<sup>49,50</sup> Compared with other nanostructured Co<sub>3</sub>O<sub>4</sub> in previous reports, our as-synthesized Co<sub>3</sub>O<sub>4</sub>@N-CNTs sample possesses outstanding high-rate and long-life cycling performance (Table S4).

Furthermore, the superior electrochemical performances are attributed to the delicate structural motifs of Co<sub>3</sub>O<sub>4</sub>@N-CNTs sample as follows. First, such a structure composed of interconnected N-CNTs can give rise to high BET specific surface area of 192 m<sup>2</sup> g<sup>-1</sup>, which efficiently enhances the electrode/electrolyte contact surface. Second, the synergistic effect between confined small Co<sub>3</sub>O<sub>4</sub> nanoparticles and outer N-CNTs provides high reaction activity, short diffusion length and fast electronic mobility. Third, the hollow interior spaces and multilevel pores in these N-CNT-assembled architectures can accommodate large volume variation and strain during the conversion reaction process.

## CONCLUSION

In summary, we have reported a facile, general and high-yield strategy for the oriented formation of CNTs by controlling the low-temperature pyrolysis of MOF crystals. This oriented formation mechanism was clearly revealed and generally applied to numerous MOFs for the first time. These architectures are effectively assembled with CNTs, which possess a large specific surface area, suitable pore size distribution, appropriate doping, interior voids and robust frameworks, resulting in high electrochemical activity, fast mass transport and good strain accommodation. As a proof-of-concept application, the N-CNT-assembled hollow structures show excellent electrochemical performance in ORR and LIBs. On the basis of experimental analyses and DFT simulations, a synergistic effect between appropriate graphitic-N doping and confined metal nanoparticles in CNTs increases the DOS near the Fermi level and reduces the work function, hence enhancing the ORR performance. Therefore, our work represents a new general approach toward the synthesis of CNTs, which will have great potential in many frontier fields.

## EXPERIMENTAL SECTION

### Synthesis of N-CNT-Assembled Dodecahedra from ZIF-67.

All the chemicals used were analytical grade and were not purified further. In a typical synthesis, cobalt nitrate hexahydrate (1.0 mmol) was dissolved in 25.0 mL of methanol. 2-Methylimidazole (4.0 mmol) was dissolved in 25.0 mL of methanol and then poured into the former pink cobalt nitrate solution. The resulting mixture was stirred for 24 h. Purple solids were collected, washed with methanol three times and dried at 70 °C in air for 6 h. The ZIF-67 precursors were then heated to 435 °C (2 °C min<sup>-1</sup>) for 8 h under an argon atmosphere. Finally, ZIF-67-derived N-CNT-assembled hollow dodecahedra (N-CNTs-435) were obtained. For comparison, the synthesized N-CNTs-435 were subsequently treated at different temperatures (550, 650, and 750 °C) for 1 h in argon, resulting in N-CNTs-550, N-CNTs-650 and N-CNTs-750, respectively. In addition, after the N-CNTs-650 sample was treated at 300 °C in air for 2 h, hollow dodecahedra assembled with Co<sub>3</sub>O<sub>4</sub> nanoparticles encapsulated into N-CNTs (Co<sub>3</sub>O<sub>4</sub>@N-CNTs) were obtained.

**Synthesis of N-CNTs-Assembled Microspheres from Co, Fe-ZIF.** Co(NO<sub>3</sub>)<sub>2</sub>·6H<sub>2</sub>O (2 mmol) and FeSO<sub>4</sub>·7H<sub>2</sub>O (0.3 mmol) were dissolved in 20 mL of *N,N*-dimethylformamide (DMF) solvent and then mixed with 2-methylimidazole (20 mL, 0.08 M) in DMF solution under stirring. The resulting mixture was stirred for another 30 min at room temperature and then transferred into a 50 mL Teflon autoclave and heated at 180 °C for 24 h. Co, Fe-ZIF microspheres were collected, washed with methanol three times and dried at 70 °C in air. Then, after complete pyrolysis at 435 °C (2 °C min<sup>-1</sup>) for 8 h in argon, Co, Fe-ZIF-derived N-CNT-assembled microspheres were obtained.

**Synthesis of N-CNT-Assembled Microspheres from Ni-ZIF.** Ni(NO<sub>3</sub>)<sub>2</sub>·6H<sub>2</sub>O (1.0 mmol) was dissolved in 20.0 mL of methanol. Imidazole (4.0 mmol) was dissolved in 20.0 mL of methanol and poured into the former solution. The resulting mixture was then stirred for 1 h. The obtained light green solution was then transferred to a 50 mL Teflon autoclave and then heated to 140 °C for 12 h. Ni-ZIF microspheres were collected, washed with methanol three times and dried at 70 °C in air. Then, after complete pyrolysis at 435 °C (2 °C min<sup>-1</sup>) for 8 h in argon, Ni-ZIF-derived N-CNT-assembled microspheres were obtained.

**Synthesis of CNT-Assembled Microsheets from Co-BTC.** Co(NO<sub>3</sub>)<sub>2</sub>·6H<sub>2</sub>O (582 mg) and trimesic acid (150 mg) were dissolved in 35 mL of DMF solvent and stirred for 2 h. The obtained light-red solution was then transferred to a 50 mL Teflon autoclave and heated to 120 °C for 24 h. Pink Co-BTC microsheets were collected, washed with methanol three times and dried at 70 °C in air. Then, after complete pyrolysis at 430 °C (2 °C min<sup>-1</sup>) for 8 h in argon, Co-BTC-derived CNT-assembled microsheets were obtained.

**Synthesis of CNT-Assembled Hollow Microspheres from Ni-BTC.** Ni(NO<sub>3</sub>)<sub>2</sub>·6H<sub>2</sub>O (432 mg), trimesic acid (150 mg), and PVP (1.5 g) were dissolved in 30 mL of a mixture solution (distilled water: ethanol: DMF = 1:1:1 v/v/v) under vigorous stirring. The obtained light green solution was then transferred to a 50 mL Teflon-lined autoclave and heated to 150 °C for 10 h. Ni-BTC hollow microspheres were collected, washed with methanol three times and dried at 70 °C in air. Then, after complete pyrolysis at 430 °C (2 °C min<sup>-1</sup>) for 8 h in argon, Ni-BTC-derived CNT-assembled hollow microspheres were obtained.

**Synthesis of CNT-Assembled Nanorods from Co-MOF.** An aqueous solution of terephthalic acid was prepared by dissolving 1.0 g of terephthalic acid in 200 mL of a 1:1 ethanol–water mixture. The organic linker solution was adjusted to pH 7 by dropwise addition of 1 M NaOH solution. An aqueous solution of Co(NO<sub>3</sub>)<sub>2</sub>·6H<sub>2</sub>O (4 mmol, 50 mL) was injected stepwise into the aforementioned mixture and stirred for 12 h. Pink Co-MOF microsheets were collected, washed with methanol three times and dried at 70 °C in air. Then, after complete pyrolysis at 430 °C (2 °C min<sup>-1</sup>) for 8 h in argon, Co-MOF-derived CNT-assembled nanorods were obtained.

**Synthesis of N-CNTs-Assembled Core–Shell Dodecahedra from Co-ZIF-67@Zn-ZIF-8.** Co(NO<sub>3</sub>)<sub>2</sub>·6H<sub>2</sub>O (1.0 mmol) was dissolved in 25.0 mL of methanol. 2-Methylimidazole (4.0 mmol)

was dissolved in 25.0 mL of methanol and then poured into the former pink solution. The mixture solution was then stirred for 24 h. Purple solids were collected, washed and dried at 70 °C in air for 6 h. The as-prepared ZIF-67 dodecahedra (20 mg) were well-dispersed in 10 mL of methanol under sonication for 0.5 h. After stirring for 0.5 h, methanolic solutions of Zn(NO<sub>3</sub>)<sub>2</sub>·6H<sub>2</sub>O (1.0 mmol, 5.0 mL) and 2-Methylimidazole (4.0 mmol, 5.0 mL) were injected stepwise into the above mixture. Co-ZIF-67@Zn-ZIF-8 dodecahedra were collected, washed with methanol three times and dried at 70 °C in air. Finally, after complete pyrolysis at 450 °C (2 °C min<sup>-1</sup>) in argon for 8 h, N-CNT-assembled core–shell dodecahedra were obtained.

**Synthesis of N-CNTs via the Traditional Solid-Phase Method.** Melamine (4.0 g) and Fe(NO<sub>3</sub>)<sub>2</sub>·9H<sub>2</sub>O (0.3 g) were dissolved in 50 mL of ethanol and stirred for 1 h. After drying at 70 °C in air, the precursor mixture was ground into a uniform powder. When the precursor mixture was treated at 435 °C (2 °C min<sup>-1</sup>) in argon for 8 h, the intermediate product was obtained. When the precursor mixture was further treated at 900 °C (2 °C min<sup>-1</sup>) in argon for 2 h, small amounts of N-CNTs were obtained.

**Synthesis of the Zn-ZIF-8 Precursor and Derived Product.** In a typical synthesis, methanolic solutions of Zn(NO<sub>3</sub>)<sub>2</sub>·6H<sub>2</sub>O (810 mg, 40 mL) and methanolic solutions of 2-methylimidazole (526 mg, 40 mL) were mixed under stirring. The resulting mixture was maintained at room temperature for 12 h. The white precipitate was centrifuged and washed several times with methanol before drying in an oven at 70 °C. In addition, when the white precipitate was treated at 600 °C (2 °C min<sup>-1</sup>) in argon for 3 h, the derived product was obtained.

**Synthesis of the Amorphous Precursor and Derived Product.** CoCl<sub>2</sub>·6H<sub>2</sub>O (5 mmol) was dissolved in 100 mL of deionized water. Then, 30 mmol of imidazole was dissolved in 100 mL of deionized water and dropped into the cobalt chloride solution. The mixture was stirred for 30 min and maintained for 8 h without disturbance. The solids were collected by centrifugation, washed with ethanol three times and dried at 70 °C in air for 6 h. Then, after treatment at 435 °C (2 °C min<sup>-1</sup>) in argon for 8 h, the derived product was obtained.

**Characterizations.** The crystallographic characteristics of the final products were measured using a Bruker D8 Discover X-ray diffractometer equipped with a Cu K $\alpha$ /Co K $\alpha$  radiation source. SEM images were collected using a JEOL-7100F scanning electron microscope, and TEM images were collected using a JEM-2100F/Titan G2 60–300 transmission electron microscope. Energy-dispersive X-ray spectra were recorded using an Oxford IE250 system. Raman and FTIR spectra were obtained using a Renishaw INVIA micro-Raman spectroscopy system. The BET surface area was calculated from nitrogen adsorption isotherms collected at 77 K using a Tristar-3020 instrument. TG-DSC-MS analysis was conducted using an STA-449F3 instrument. XPS and UPS measurements were conducted using an ESCALAB 250Xi instrument.

**Electrocatalysis Measurements.** For the ORR, the electrocatalytic activities of catalysts toward the ORR were measured in O<sub>2</sub>-saturated 0.1 M KOH aqueous solution, with a saturated calomel reference electrode (SCE), a Pt wire counter electrode, and a working electrode. An ink of the catalyst was prepared by mixing 8 mg of catalyst powder and 2 mg of Vulcan XC72R (VXC72R) with 50  $\mu$ L of a 5 wt % Nafion solution, 200  $\mu$ L of deionized water, and 750  $\mu$ L of isopropanol, and placing the resulting mixture in an ultrasonic bath. Cyclic voltammograms at a sweep rate of 5 mV s<sup>-1</sup> were recorded in the potential range from 0.1 to –0.8 V versus SCE. LSV was performed in O<sub>2</sub>-saturated 0.1 M KOH. ORR polarization curves were recorded at a scan rate of 5 mV s<sup>-1</sup> under various electrode rotation rates (400, 625, 900, 1225, 1600, and 2250 rpm). The Pt ring potential was set at 0.5 V versus SCE to monitor the formation of peroxide species. All the potentials were converted to the RHE potential scale.

Before each measurement, the 0.1 M KOH electrolyte was bubbled with O<sub>2</sub> for more than 30 min. RRDE measurements were performed at 1600 rpm using a CHI 760 E electrochemical workstation equipped with an RRDE-E7R9 rotator (Pine Co., Ltd.).

The ORR kinetics were analyzed using the Koutecky–Levich (K–L) equation

$$\frac{1}{i} = \frac{1}{i_k} + \frac{1}{i_d} = -\frac{1}{nFAkC^0} - \frac{1}{0.62nFAD_{O_2}^{2/3}v^{-1/6}C^0\omega^{1/2}} \quad (1)$$

where  $i$ ,  $i_k$ , and  $i_d$  correspond to the measured, kinetic, and diffusion-limiting currents, respectively;  $n$  is the overall transferred electron number;  $F$  is the Faraday constant;  $A$  is the geometric electrode area ( $\text{cm}^2$ );  $k$  is the rate constant for oxygen reduction;  $C^0$  is the saturated concentration of oxygen in 0.1 M KOH;  $D_{O_2}$  is the diffusion coefficient of oxygen;  $v$  is the kinetic viscosity of the solution; and  $\omega$  is the rotation rate ( $\text{rad}\cdot\text{s}^{-1}$ ) of the electrode. Further, the percentage of peroxide species ( $\text{HO}_2^-$ ) with respect to the total generated oxygen reduction products and the electron reduction number ( $n$ ) were calculated as

$$\text{HO}_2^- = 200 \frac{I_r/N}{I_d + I_r/N} \quad (2)$$

$$n = 4 \frac{I_d}{I_d + I_r/N} \quad (3)$$

where  $I_d$  is the disk current,  $I_r$  is the ring current, and  $N$  is the current collection efficiency (0.37) of the RRDE.

All potentials were calibrated with respect to RHE scale according to the Nernst equation ( $E_{\text{RHE}} = E_{\text{SCE}} + 0.059 \times \text{pH} + 0.245 \text{ V}$ ).

**Computational Details.** All simulations on carbon nanotubes were based on density functional theory (DFT) and carried out by using the projector augmented wave method (PAW) as implemented in the Vienna ab initio simulation package (VASP).<sup>51,52</sup> The exchange and correlation functional was treated as generalized gradient approximation (GGA) of the Perdew–Burke–Ernzerhof (PBE) formula.<sup>53</sup> The wave functions were expanded by using the plane waves up to a kinetic energy cutoff of 500 eV. Brillouin-zone integrations were approximated by using special  $k$ -point sampling of Monkhorst–Pack scheme with a  $k$ -point mesh resolution of  $2\pi \times 0.03 \text{ \AA}^{-1}$ .<sup>54</sup> The unit cell lattice vectors (unit cell shape and size) and atomic coordinates were fully relaxed until the force on each atom was less than  $0.02 \text{ eV \AA}^{-1}$ .

**Lithium Storage Measurements.** The anode electrodes were composed of 80 wt %  $\text{Co}_3\text{O}_4$ @N-CNTs, 10 wt % acetylene black, and 10 wt % carboxymethyl cellulose (CMC) binder. After coating onto copper foil, the electrode film was uniformly cut into  $\sim 0.5 \text{ cm}^2$  (area) round slices, weighing a total of  $\sim 1.2 \text{ mg}$ ; the corresponding areal mass loading was  $2.4 \text{ mg}\cdot\text{cm}^{-2}$ . 2,016 coin cells were assembled in a glovebox filled with pure argon gas. Lithium foil was used as the counter electrode and the separator was Celgard 2400 microporous membrane. One M lithium hexafluorophosphate ( $\text{LiPF}_6$ ) solution in ethylene carbon (EC)-dimethyl carbonate (DMC) (1:1 v/v) was used as the electrolyte. Galvanostatic charge–discharge measurements were performed using a multichannel battery testing system (LAND CT2001A). CVs and electrochemical impedance spectra were collected at room temperature using an Autolab potentiostat/galvanostat. The capacity was based on the total mass of  $\text{Co}_3\text{O}_4$ @N-CNTs composites.

## ■ ASSOCIATED CONTENT

### Supporting Information

The Supporting Information is available free of charge on the ACS Publications website at DOI: 10.1021/jacs.7b01942.

Schematic illustration, yields of various products, crystal parameters, details of XRD, XPS, SEM, TEM, FT-IR, Raman, BET surface area, Elemental mapping images and DFT simulation results (PDF)

## ■ AUTHOR INFORMATION

### Corresponding Authors

\*zzhu@xmu.edu.cn

\*mlq518@whut.edu.cn

### ORCID

Zizhong Zhu: 0000-0001-5353-4418

Dongyuan Zhao: 0000-0001-8440-6902

Liqiang Mai: 0000-0003-4259-7725

### Author Contributions

#J.M., C.N., and L.X. contributed equally to this work.

### Notes

The authors declare no competing financial interest.

## ■ ACKNOWLEDGMENTS

This work was supported by the National Key Research and Development Program of China (2016YFA0202603), the National Basic Research Program of China (2013CB934103), the Programme of Introducing Talents of Discipline to Universities (B17034), the National Natural Science Foundation of China (51521001), the National Natural Science Fund for Distinguished Young Scholars (51425204), and the Fundamental Research Funds for the Central Universities (WUT: 22016III001 and 2016-YB-004). We thank Prof. C. W. Nan of Tsinghua University for useful discussions and assistance with the manuscript. We are grateful to Bichao Xu and Pei Zhang of the Core Facility and Technical Support, Wuhan Institute of Virology for her technical support in transmission electron microscopy. Prof. Liqiang Mai gratefully acknowledged financial support from China Scholarship Council (No. 201606955096). All authors read and commented on the manuscript.

## ■ REFERENCES

- Iijima, S. *Nature* **1991**, *354*, 56–58.
- Baughman, R. H.; Zakhidov, A. A.; de Heer, W. A. *Science* **2002**, *297*, 787–792.
- Zhou, M.; Wang, H. L.; Guo, S. J. *Chem. Soc. Rev.* **2016**, *45*, 1273–1307.
- Sgobba, V.; Guldi, D. M. *Chem. Soc. Rev.* **2009**, *38*, 165–184.
- De Volder, M. F.; Tawfick, S. H.; Baughman, R. H.; Hart, A. J. *Science* **2013**, *339*, 535–539.
- Zhu, H. W.; Xu, C. L.; Wu, D. H.; Wei, B. Q.; Vajtai, R.; Ajayan, P. M. *Science* **2002**, *296*, 884–886.
- Ajayan, P. M. *Chem. Rev.* **1999**, *99*, 1787–1800.
- Segawa, Y.; Ito, H.; Itami, K. *Nat. Rev. Mater.* **2016**, *1*, 15002.
- Gong, K.; Du, F.; Xia, Z.; Durstock, M.; Dai, L. M. *Science* **2009**, *323*, 760–764.
- Omachi, H.; Segawa, Y.; Itami, K. *Acc. Chem. Res.* **2012**, *45*, 1378–1389.
- Hitosugi, S.; Nakanishi, W.; Yamasaki, T.; Isobe, H. *Nat. Commun.* **2011**, *2*, 492.
- Shrestha, L. K.; Sathish, M.; Hill, J. P.; Miyazawa, K.; Tsuruoka, T.; Sanchez-Ballester, N. M.; Honma, I.; Ji, Q. M.; Ariga, K. *J. Mater. Chem. C* **2013**, *1*, 1174–1181.
- Bairi, P.; Minami, K.; Nakanishi, W.; Hill, J. P.; Ariga, K.; Shrestha, L. K. *ACS Nano* **2016**, *10*, 6631–6637.
- Wei, B. Q.; Vajtai, R.; Jung, Y.; Ward, J.; Zhang, R.; Ramanath, G.; Ajayan, P. M. *Nature* **2002**, *416*, 495–496.
- Dai, L. M.; Xue, Y. H.; Qu, L. T.; Choi, H. J.; Baek, J. B. *Chem. Rev.* **2015**, *115*, 4823–4892.
- Jiao, Y.; Zheng, Y.; Davey, K.; Qiao, S. Z. *Nat. Energy* **2016**, *1*, 16130.
- Stock, N.; Biswas, S. *Chem. Rev.* **2011**, *112*, 933–969.
- Howarth, A. J.; Liu, Y. Y.; Li, P.; Li, Z. Y.; Wang, T. C.; Hupp, J. T.; Farha, O. K. *Nat. Rev. Mater.* **2016**, *1*, 15018.
- Sakaushi, K.; Antonietti, M. *Bull. Chem. Soc. Jpn.* **2015**, *88*, 389–398.
- Yamada, T.; Sadakiyo, M.; Shigematsu, A.; Kitagawa, H. *Bull. Chem. Soc. Jpn.* **2016**, *89*, 1–10.

- (21) Lu, W. G.; Wei, Z. W.; Gu, Z. Y.; Liu, T. F.; Park, J.; Park, J.; Tian, J.; Zhang, M. W.; Ill, T. G.; Bosch, M.; Zhou, H. C. *Chem. Soc. Rev.* **2014**, *43*, 5561–5593.
- (22) Mahmood, A.; Guo, W. H.; Tabassum, H.; Zou, R. Q. *Adv. Energy Mater.* **2016**, *6*, 1600423.
- (23) Xia, W.; Mahmood, A.; Zou, R. Q.; Xu, Q. *Energy Environ. Sci.* **2015**, *8*, 1837–1866.
- (24) Chen, L. Y.; Bai, J. F.; Wang, C. Z.; Pan, Y.; Scheer, M.; You, X. Z. *Chem. Commun.* **2008**, *13*, 1581–1583.
- (25) Xia, B. Y.; Yan, Y.; Li, N.; Wu, H. B.; Lou, X. W.; Wang, X. Nat. *Energy* **2016**, *1*, 15006.
- (26) Pachfule, P.; Shinde, D.; Majumder, M.; Xu, Q. *Nat. Chem.* **2016**, *8*, 718–724.
- (27) Hu, H.; Han, L.; Yu, M. Z.; Wang, Z. Y.; Lou, X. W. *Energy Environ. Sci.* **2016**, *9*, 107–111.
- (28) Pang, Q.; Tang, J. T.; Huang, H.; Liang, X.; Hart, C.; Tam, K. C.; Nazar, L. F. *Adv. Mater.* **2015**, *27*, 6021–6028.
- (29) Huang, Z. F.; Song, J. J.; Li, K.; Tahir, M.; Wang, Y. T.; Pan, L.; Wang, L.; Zhang, X. W.; Zou, J. J. *J. Am. Chem. Soc.* **2016**, *138*, 1359–1365.
- (30) Zou, F.; Chen, Y. M.; Liu, K. W.; Yu, Z. T.; Liang, W. F.; Bhaway, S. M.; Gao, M.; Zhu, Y. *ACS Nano* **2015**, *10*, 377–386.
- (31) Li, C.; Chen, T. Q.; Xu, W. J.; Lou, X. B.; Pan, L. K.; Chen, Q.; Hu, B. W. *J. Mater. Chem. A* **2015**, *3*, 5585–5591.
- (32) Tang, J.; Salunkhe, R. R.; Liu, J.; Torad, N. L.; Imura, M.; Furukawa, S.; Yamauchi, Y. *J. Am. Chem. Soc.* **2015**, *137*, 1572–1580.
- (33) Zhang, C. H.; Fu, L.; Liu, N.; Liu, M. H.; Wang, Y. Y.; Liu, Z. F. *Adv. Mater.* **2011**, *23*, 1020–1024.
- (34) Mai, L. Q.; Tian, X. C.; Xu, X.; Chang, L.; Xu, L. *Chem. Rev.* **2014**, *114*, 11828–11862.
- (35) Liu, X. E.; Dai, L. M. *Nat. Rev. Mater.* **2016**, *1*, 16064.
- (36) Liang, Y. Y.; Li, Y. G.; Wang, H. L.; Zhou, J. G.; Wang, J.; Regier, T.; Dai, H. J. *Nat. Mater.* **2011**, *10*, 780–786.
- (37) Wu, Z. Y.; Xu, X. X.; Hu, B. C.; Liang, H. W.; Lin, Y.; Chen, L. F.; Yu, S. H. *Angew. Chem., Int. Ed.* **2015**, *54*, 8179–8183.
- (38) Wang, Z. L.; Xu, D.; Zhong, H. X.; Wang, J.; Meng, F. L.; Zhang, X. B. *Sci. Adv.* **2015**, *1*, e1400035.
- (39) Hu, C. G.; Dai, L. M. *Angew. Chem., Int. Ed.* **2016**, *55*, 11736–11758.
- (40) Deng, D. H.; Yu, L.; Chen, X. Q.; Wang, G. X.; Jin, L.; Pan, X. L.; Deng, J.; Sun, G. Q.; Bao, X. H. *Angew. Chem., Int. Ed.* **2013**, *52*, 371–375.
- (41) Shao, M. H.; Chang, Q. W.; Dodelet, J. P.; Chenitz, R. *Chem. Rev.* **2016**, *116*, 3594–3657.
- (42) Yang, H. B.; Miao, J. W.; Hung, S. F.; Chen, J. Z.; Tao, H. B.; Wang, X. Z.; Zhang, L. P.; Chen, R.; Gao, J. J.; Chen, H. M.; Dai, L. M.; Liu, B. *Sci. Adv.* **2016**, *2*, e1501122.
- (43) Lai, L. F.; Potts, J. R.; Zhan, D.; Wang, L.; Poh, C. K.; Tang, C. H.; Gong, H.; Shen, Z. X.; Lin, J. Y.; Ruoff, R. S. *Energy Environ. Sci.* **2012**, *5*, 7936–7942.
- (44) Cheon, J. Y.; Kim, J. H.; Kim, J. H.; Goddeti, K. C.; Park, J. K.; Joo, S. H. *J. Am. Chem. Soc.* **2014**, *136*, 8875–8878.
- (45) Kim, H.; Lee, K.; Woo, S. I.; Jung, Y. *Phys. Chem. Chem. Phys.* **2011**, *13*, 17505–17510.
- (46) Guo, D. H.; Shibuya, R.; Akiba, C.; Saji, S.; Kondo, T.; Nakamura, J. *Science* **2016**, *351*, 361–365.
- (47) Choi, C. H.; Lim, H. K.; Chung, M. W.; Park, J. C.; Shin, H.; Kim, H.; Woo, S. I. *J. Am. Chem. Soc.* **2014**, *136*, 9070–9077.
- (48) Palacin, M. R. *Chem. Soc. Rev.* **2009**, *38*, 2565–2575.
- (49) Niu, C. J.; Meng, J. S.; Wang, X. P.; Han, C. H.; Yan, M. Y.; Zhao, K. N.; Xu, X. M.; Ren, W. H.; Zhao, Y. L.; Xu, L.; Zhang, Q. J.; Zhao, D. Y.; Mai, L. Q. *Nat. Commun.* **2015**, *6*, 7402.
- (50) Li, Y. Z.; Yan, K.; Lee, H. W.; Lu, Z. D.; Liu, N.; Cui, Y. *Nat. Energy* **2016**, *1*, 15029.
- (51) Kresse, G.; Joubert, D. *Phys. Rev. B: Condens. Matter Mater. Phys.* **1999**, *59*, 1758.
- (52) Kresse, G.; Furthmüller, J. *Comput. Mater. Sci.* **1996**, *6*, 15–50.
- (53) Perdew, J. P.; Burke, K.; Ernzerhof, M. *Phys. Rev. Lett.* **1996**, *77*, 3865–3868.
- (54) Monkhorst, H. J.; Pack, J. D. *Phys. Rev. B* **1976**, *13*, 5188–5192.